

DARK MATTER ADMIXED TYPE IA SUPERNOVAE

S.-C. LEUNG, M.-C. CHU, AND L.-M. LIN

Department of Physics and Institute of Theoretical Physics, The Chinese University of Hong Kong, Hong Kong S.A.R., China

(Dated: January 1, 2020)

Draft version January 1, 2020

ABSTRACT

We perform two-dimensional hydrodynamic simulations for the thermonuclear explosion of Chandrasekhar-mass white dwarfs with dark matter (DM) cores in Newtonian gravity. We include a 19-isotope nuclear reaction network and make use of the pure turbulent deflagration model as the explosion mechanism in our simulations. Our numerical results show that the general properties of the explosion depend quite sensitively on the mass of the DM core M_{DM} : a larger M_{DM} generally leads to a weaker explosion and a lower mass of synthesized iron-peaked elements. In particular, the total mass of ^{56}Ni produced can drop from about 0.3 to $0.03M_{\odot}$ as M_{DM} increases from 0.01 to $0.03M_{\odot}$. We have also constructed the bolometric light curves obtained from our simulations and found that our results match well with the observational data of sub-luminous Type-Ia supernovae.

1. INTRODUCTION

1.1. *Type-Ia supernovae*

Type-Ia supernovae (SNIa) are important astrophysical objects because of the similarity in their light curves and spectra (Branch & Tammann 1992), which leads to wide applications of SNIa in cosmological distance measurement such as the determination of the Hubble parameters (Leibundgut & Pinto 1992) and the discovery of the accelerating expansion of the universe (Riess et al. 1998; Perlmutter et al. 1999). However, despite their important roles in modern cosmology, both the progenitor system and explosion mechanism of SNIa are not yet fully understood. While it is generally believed that SNIa are due to the thermonuclear explosion of a carbon-oxygen white dwarf (WD) in binary systems, it is still unclear whether the companion is a normal non-degenerate star or another WD. Traditionally, SNIa is attributed to the explosion of a WD at the Chandrasekhar mass limit (Arnett 1969). The WD has a mass initially far from the mass limit. Depending on the accretion rate, the mass can either gradually grow until the baryonic matter becomes degenerate (Nomoto 1982a), or a detonation front forms at the envelope and sheds away the outer mass (Nomoto 1982b). Both mechanisms provide conditions for the formation of a first trigger (Nomoto et al. 1984) which spreads in the form of a deflagration wave (Nomoto et al. 1976) and unbinds the star. However, neither pure deflagration (Nomoto et al. 1984) nor pure detonation model (Arnett 1969) is adequate to explain the observed velocity profile, optical light curve, spectra, galactic chemical abundance and explosion strength. Furthermore, recent studies show that SNIa can be formed without invoking Chandrasekhar mass WD (Scalzo et al. 2014). For example, violent white dwarf mergers can also explain the SNIa distributions (Pakmor et al. 2013).

The difficulties encountered by the pure deflagration and pure detonation models have led to extensions of models including the pure turbulent deflagration (PTD) model (Reinecke et al. 1999a,b, 2002a,b), delayed-detonation transition (DDT) model (Khoholov 1989; Khokhlov 1991a,b,c; Khokhlov et al. 1997) and

gravitationally confined detonation (GCD) model (previously known as the detonation failed deflagration model) (Plewa 2007; Kasen & Plewa 2007; Jordan et al. 2008; Meakin et al. 2009; Jordan et al. 2012). Each model has its own theoretical difficulties. For example, while the PTD model can produce explosion with a variety of strengths (Roepke et al. 2006), there are still unburnt low-velocity carbon and oxygen near the core, which are not observed (Roepke et al. 2007). The DDT model can provide sufficient intermediate mass elements (IME) and leave very little fuel (Gamezo et al. 2004, 2005). However, the possibility of transition is still being debated (Lisewski et al. 2000).

In recent years, the PTD, DDT and GCD models are studied extensively in multi-dimensional simulations (Long et al. 2014; Seitenzahl et al. 2013; Jordan et al. 2012). The models can well explain the phenomena of normal SNIa, i.e., supernovae with a correlated peak luminosity against B-band decline rate, chemical stratification and a large velocity gradient (Benetti et al. 2005). However, there is a significant number of peculiar SNIa which are sub-luminous and super-luminous (Li et al. 2001). In particular, sub-luminous SNIa have a much lower absolute magnitude of B-band at maximum. For example, the famous SN1991bg (Filippenko et al. 1992) recorded a 2.5 mag and 1.6 mag dimmer in B- and V-band peak magnitudes. The B-band decline rate is faster than the norm, with a lower expansion velocity and stronger Si II absorption lines (Doull & Baron 2011). It was initially assumed that such unusual SNIa are extremely rare. However, there are now sufficient number of sub-luminous SNIa that they are classified as the FAINT group as suggested in (Benetti et al. 2005). Detailed study shows that the light curves in this group of SNIa are also homogeneous among themselves as those of normal SNIa (Doull & Baron 2011). The faintest SNIa ever found to date is SN2008ha (Foley et al. 2009), with a low magnitude of $M_V = -14.2$ mag and extremely low expansion velocity ~ 2000 km s⁻¹.

In view of the discovery of sub-luminous and super-luminous SNIa, the explosion of a Chandrasekhar-mass WD can no longer be the sole explanation of SNIa

because of the lack of variety in its explosion. The sub-Chandrasekhar mass double detonation model is often regarded as the explanation for sub-luminous SNIa (Woosley & Weaver 1994). The model suggests that when the mass accretion of a WD from its companion is adequately fast, the matter on its envelope, mostly helium, can be ignited and an implosion is triggered (Nomoto 1982b). The front converges at the WD core and a second explosion is created. This model allows a WD to be burnt if the matter is not yet degenerate. By tuning the host WD mass, less luminous SNIa can be modeled, which can be fitted to explain certain sub-luminous SNIa, for instance SN1991bg (Ruiz-Lapuente et al. 1993). The helium detonation is found robust in inducing a second explosion (Fink et al. 2009) and the predicted optical signal is compatible with observations (Kromer et al. 2010; Sim et al. 2012). However, recent studies of this model with less massive helium shell show similar features as normal SNIa (Sim 2010; Ruiter et al. 2011, 2014) instead of sub-luminous ones. Furthermore, the detonation might not be started robustly (Livne & Glasner 1990). Even when a helium detonation is triggered, the detonation wave might not penetrate deep into the carbon/oxygen core (Moll & Woosley 2013), and the distribution of outer chemical elements can be in conflict with observation data (Hoefflich & Khokhlov 1996; Hoefflich et al. 1996).

Another popular proposal for explaining sub-luminous SNIa is the pure turbulent deflagration model with remnant. This model assumes that the deflagration only partially burns the WD, and parts of the WD remain bounded after the explosion. It is applied to the SN2002cx class of the sub-luminous SNIa. The synthetic color light curves and the spectra can match well with the observational data (Jordan et al. 2012; Kromer et al. 2013a; Fink et al. 2014). In (Kromer et al. 2015) this model is further shown to be in good agreement with the faintest SN2008ha. The recent observational hints of the SN2008ha remnant (Foley et al. 2014) also support this model as the origin of this class of sub-luminous SNIa.

Violent merging of two low-mass WD's is also a possible candidate of explaining the sub-luminous SNIa. For example, (Pakmor et al. 2010) showed that this model provides a good match to the observed features of SN1991bg, while in (Kromer et al. 2013b) the light curves and spectra of SN2010lp are well reproduced.

1.2. Dark matter astrophysics

The effects of various dark matter (DM) candidates on stellar evolution and structure have been studied in details. For example, the effects of DM annihilation as the energy source in early stars have been considered in (Spolyar et al. 2008; Ripamonti et al. 2010; Fairbairn et al. 2008; Freese et al. 2009; Spolyar et al. 2009; Hirano et al. 2011). The DM particle capture and evaporation rates of the sun (Gould 1987a,b) and the Earth (Gould 1988) were studied in early 1990s. The dense core of compact stars is also a good probe of DM (Bertone & Fairbairn 2008; Fan et al. 2011; de Lavallaz & Fairbairn 2010). DM particles can annihilate or decay inside a compact star and thus provide an energy source (Gonzalez & Reisenegger 2010; Perez-Garcia & Silk 2014). For example, it has been suggested that the energy is sufficient to maintain

the surface temperature of WDs (Moskalenko & Wai 2007; Hooper et al. 2012) and neutron stars (Kouvaris 2008; Kouvaris & Tinyakov 2010). On the other hand, non-self-annihilating DM can affect the star by its gravity. The self-gravitating DM core inside a compact star might collapse, which forms a black hole and engulfs the star (Goldman & Nussinov 1989; de Lavallaz & Fairbairn 2010). The detection of ancient compact stars can thus provide limits on the DM scattering cross section for different types of DM particles (Kouvaris & Tinyakov 2011; Kouvaris 2012; McDermott et al. 2012; Bramante et al. 2013).

1.3. Motivation

Previously, we have studied the equilibrium structure and stability of compact stars with cores composed of non-self-annihilating DM particles which are modeled by an ideal Fermi gas (Leung et al. 2011, 2012, 2013). In particular, for DM particle mass of about 1 GeV, we found that the DM core can affect the structure of a WD significantly. The DM core can be as massive as about $0.01M_{\odot}$ and the Chandrasekhar mass limits of these WD can be smaller than those without DM by as much as 40%. An implication of our findings in (Leung et al. 2013) is that the initial conditions of SNIa might not be as universal as generally assumed. In this paper, we study how DM affects SNIa explosions by performing two-dimensional hydrodynamic simulations of the thermonuclear explosions of Chandrasekhar-mass WDs with DM cores. We find that these objects generally have weaker explosions and lower masses of synthesized iron-peaked elements, and hence they may account for the sub-luminous class of SNIa.

The plan of this paper is as follows: In Section 2 we outline the equations and methods that we used in the numerical simulations. Section 3 presents the general results of our SNIa simulations in terms of the explosion energy, nucleosynthesis, and features of the propagating flame surface. We also compare the bolometric light curves constructed from our simulations with the observational data of sub-luminous SNIa. Finally, we summarize in section 4.

2. METHODS

We have developed a two-dimensional hydrodynamical code with Newtonian gravity to model SNIa. The code makes use of the Weighted Essential Non-Oscillatory (WENO) scheme for spatial discretization (Barth & Deconinck 1999). This is a fifth-order scheme which processes piecewise smooth functions with discontinuities in order to simulate the flux across grid cells with high precision, while avoiding spurious oscillations around the shock. The discretization in time is performed by using the five-stage, third-order, non-strong stability preserving explicit Runge-Kutta scheme (Barth & Deconinck 1999). Various consistency and convergence tests have been done to validate our code (Leung et al. 2015). Here we only outline the essence of the code.

2.1. Initial Model

In the simulation there are both baryonic normal matter (NM) and DM. The initial density profiles are obtained by solving the hydrostatic equilibrium equations

for both NM and DM:

$$\frac{dp_{\text{NM}}}{dr} = -\frac{G(M_{c(\text{NM})}(r) + M_{c(\text{DM})}(r))}{r^2} \rho_{\text{NM}}, \quad (1)$$

$$\frac{dp_{\text{DM}}}{dr} = -\frac{G(M_{c(\text{NM})}(r) + M_{c(\text{DM})}(r))}{r^2} \rho_{\text{DM}}, \quad (2)$$

where ρ_{NM} and ρ_{DM} are the NM and DM density, respectively. The enclosed masses of $M_{c(\text{NM})}$ and $M_{c(\text{DM})}$ are determined by

$$\frac{dM_{c(\text{NM})}}{dr} = 4\pi r^2 \rho_{\text{NM}}, \quad (3)$$

$$\frac{dM_{c(\text{DM})}}{dr} = 4\pi r^2 \rho_{\text{DM}}. \quad (4)$$

The initial NM is assumed to be isothermal with a temperature of 10^8 K. The chemical composition is 50% ^{12}C and 50% ^{16}O by mass. To construct the initial WD models and simulate the NM dynamics, we employ the equation of state (EOS) developed and calibrated in (Timmes & Arnett 1999; Timmes & Swesty 1999). The EOS describes the equilibrium thermodynamics properties of a gas which includes 1. electrons in the form of an ideal gas with arbitrarily degenerate and relativistic levels, 2. ions in the form of a classical ideal gas, 3. photons described by the Planck distribution, 4. contributions from electron-positron pairs. On the other hand, the DM is modeled by an ideal degenerate Fermi gas with a particle mass m_{DM} of 1 - 10 GeV (Leung et al. 2011, 2012, 2013), which is motivated by recent hints on possible detection of GeV scale DM particles in some direct DM searches, such as DAMA and CoGeNT (Bernabei et al. 2013; Aalseth & others 2011). One concern is that the admixed DM core may alter the stellar evolution path during the main-sequence stage, where deviations from standard stellar evolution theory have not been observed. We show in the Appendix that the range of M_{DM} considered does not bring significant effects on the evolution tracks, especially of the carbon-oxygen WD progenitors, namely 4 - 7 M_{\odot} main-sequence stars.

We plot in Fig. 1 the density profiles of two of our initial models with $m_{\text{DM}} = 1$ GeV. The upper panel of Fig. 1 is a standard model without DM (Model 2D-PTD-3-0-c3 in Table 1). The lower panel shows the NM and DM profiles of a stellar model with a DM core of mass $M_{\text{DM}} = 0.03M_{\odot}$ (Model 2D-PTD-3-3-c3 in Table 1). The central DM density of this model is about 3 orders of magnitude higher than that of the NM. Due to its high compactness, the DM core produces a strong gravitational field around the core region and leads to a cusp-like structure in NM and steep NM density gradient in the core. We remark that the density profiles shown here are different from those in (Leung et al. 2013) owing to the choice of DM particle mass and the total mass of admixed DM. In Fig. 6 of (Leung et al. 2013) the EOS of DM particle is chosen to be 10 GeV ideal degenerate Fermi gas instead of 1 GeV in this article. Also, in the same figure of (Leung et al. 2013), the admixed DM mass is about $10^{-3}M_{\odot}$, which is one order of magnitude lower than those in Fig. 1.

2.2. Hydrodynamics

The thermonuclear explosion of a WD with a DM core is inherently a two-fluid system where the NM and DM

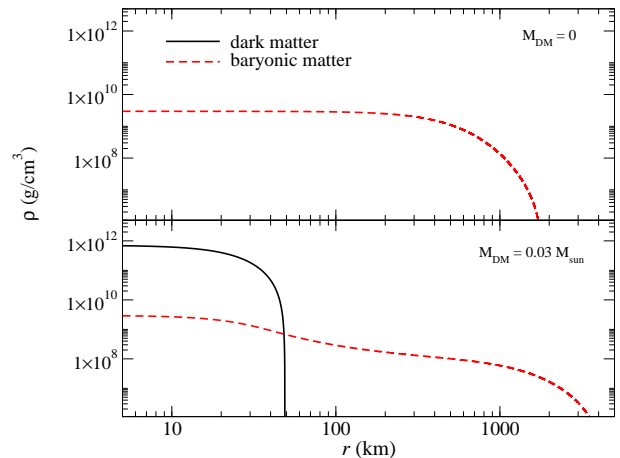


Figure 1. Upper panel: initial NM density profile of Model 2D-PTD-3-0-c3 listed in Table 1. Lower panel: initial NM (dashed line) and DM (solid line) density profiles of Model 2D-PTD-3-3-c3.

couple through gravity. In principle, one has to model the dynamics of the two fluids consistently by solving two different sets of hydrodynamics equations. However, the typical density of DM in our simulations is about two or three orders of magnitude higher than that of NM. The size of the DM core is also much smaller than the stellar radius. As a result, the dynamical time and length scales of NM and DM differ by orders of magnitude, and hence performing a consistent and accurate two-fluid hydrodynamics simulation for SNIa would be a computationally challenging task. On the other hand, due to its high compactness, the dynamics of the DM core is governed mainly by its self-gravity. The motion of NM near the core is influenced by the DM, but not vice versa. Furthermore, the total energy release and nucleosynthesis in the explosion depend mainly on the propagation of the flame, which lies well outside the DM core. It may thus be reasonable to neglect the motion of DM in the explosion.

As a first step towards understanding the effects of DM on SNIa explosions, we only model the dynamics of NM in the simulations. The DM core is assumed to be stationary and affects the NM only through its gravitational field. The hydrodynamic code solves the two-dimensional Euler equations for NM in cylindrical coordinates (r, z) with a detailed nuclear reaction network coupled with sub-grid turbulence. The equations are

$$\frac{\partial \rho_{\text{NM}}}{\partial t} + \nabla \cdot (\rho \vec{v}) = 0, \quad (5)$$

$$\frac{\partial (\rho_{\text{NM}} \vec{v})}{\partial t} + \nabla \cdot (\rho \vec{v} \vec{v}) = -\nabla P - \rho \nabla \Phi, \quad (6)$$

$$\frac{\partial \tau}{\partial t} + \nabla \cdot [\vec{v}(\tau + p)] = \rho \vec{v} \cdot \nabla \Phi + Q_{\text{nuc}} - Q_{\text{turb}} - Q_{\nu}, \quad (7)$$

$$\frac{\partial (\rho_{\text{NM}} q)}{\partial t} + \nabla \cdot (\rho_{\text{NM}} q \vec{v}) = Q_{\text{turb}} + \nabla \cdot (\rho_{\text{NM}} \nu_{\text{turb}} \nabla q), \quad (8)$$

where ρ_{NM} , v_r , v_z , p_{NM} and τ are the mass density, velocities in the r and z directions, pressure and total energy density of the baryonic matter. The total energy den-

sity includes both the thermal and kinetic contributions $\tau = \rho_{\text{NM}}\epsilon + \frac{1}{2}\rho_{\text{NM}}v^2$, where ϵ is the specific internal energy. The specific turbulence energy q is determined by Eq. (8). The gravitational potential Φ is sourced by both fluids and is determined by the Poisson equation

$$\nabla^2\Phi = 4\pi G(\rho_{\text{NM}} + \rho_{\text{DM}}). \quad (9)$$

In Eqs. (7) and (8), Q_{nuc} and Q_{turb} are the heat sources from nuclear fusions and sub-grid turbulence, respectively; Q_ν is the heat loss due to neutrino emission, and ν_{turb} is the effective eddy viscosity. We refer the reader to (Niemeyer & Hillebrandt 1995; Reinecke et al. 2002a) for a detailed discussion on how these quantities are determined in the simulations. To calculate the heat production from nuclear reactions, we incorporate the 19-isotope nuclear reaction network subroutine developed by Timmes (1999) into our hydrodynamic code. The isotopes include ^1H , ^3He , ^4He , ^{12}C , ^{14}N , ^{16}O , ^{20}Ne , ^{24}Mg , ^{28}Si , ^{32}S , ^{36}Ar , ^{40}Ca , ^{44}Ti , ^{48}Cr , ^{52}Fe , ^{54}Fe , ^{56}Ni , neutron and proton. The fusion network includes reactions starting from hydrogen burning up to silicon burning. Reactions of (α, γ) and $(\alpha, p)(p, \gamma)$ are also included.

We employ the PTD model as the explosion mechanism using the standard configurations that have been considered in the literature. In particular, an initial flame of shape *c3* is imposed for all the simulation models and the propagation of the flame is modeled by the standard level-set method (see Reinecke et al. (1999a) for details). Finally, we also construct the theoretical light curves from our simulation data by using the analytical model for SNIa (Arnett 1982), which assumes the photon diffusion limit. This model takes three input parameters: the ejecta mass M_{ej} , ejecta velocity v_{ej} and the nickel mass M_{Ni} , which can be derived from the simulation results. We also employ the opacity $\kappa = 0.1 \text{ g}^{-1}\text{cm}^2$ and the gamma-ray deposition function according to Arnett (1982).

3. RESULTS

3.1. General properties

In our simulations, the central density of NM is fixed to be $\rho_{c(\text{NM})} = 3 \times 10^9 \text{ g cm}^{-3}$ because it is expected that the minimum density needed for triggering the thermonuclear explosion is about $2 - 5 \times 10^9 \text{ g cm}^{-3}$ (Iwamoto et al. 1999; Woosley 1997; LeSaffre et al. 2006; Seitenzahl et al. 2011). We treat the DM core mass M_{DM} as a parameter in the simulations, and we assume $m_{\text{DM}} = 1 \text{ GeV}$ unless otherwise noted.

The properties of four of our typical simulation models are listed in Table 1, where $\rho_{c(\text{NM})}$ ($\rho_{c(\text{DM})}$) and M_{NM} (M_{DM}) are the central density and total mass of NM (DM), respectively. R is the initial stellar radius. The first model 2D-PTD-3-0-c3 in the table represents a standard model without DM. The other three models in the table have different DM core masses ranging from $M_{\text{DM}} = 0.01$ to $0.03M_\odot$. All these configurations are very close to the corresponding Chandrasekhar-mass limits for the given M_{DM} . The resulting mass of ^{56}Ni , energy released through nuclear reactions E_{nuc} , and total energy E_{tot} are also presented in the table. For the same central density of NM, the baryonic mass of the star decreases as M_{DM} increases. However, the (baryonic) radius of the star increases with M_{DM} .

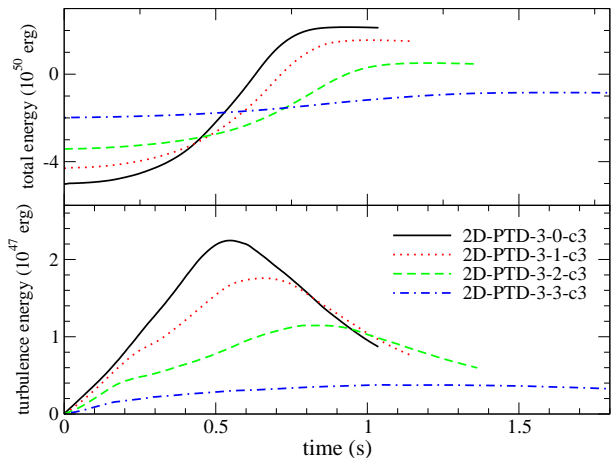


Figure 2. Upper panel: total energy against time for the models listed in Table 1. Lower panel: same as above, but for the total turbulence energy.

In the upper panel of Fig. 2 we plot the total energy for the models listed in Table 1. Note that for a fixed central NM density, the total NM mass M_{NM} decreases as M_{DM} increases. As a result, the initial total energy increases with M_{DM} because most of the binding energy is contributed by NM. At early time, models with less DM have faster energy growth than those with a more massive DM core. The total energy released, by comparing the initial and final energies, decreases when M_{DM} increases. For Model 2D-PTD-3-3-c3, the effects of the admixed DM core are so large that the WD remains bound at the end of the simulation due to its much lower energy release. In the lower panel of Fig. 2, we plot the total turbulence kinetic energy against time for the same models. Similar to the total energy released, the sub-grid turbulence energy drops when M_{DM} increases. The upper panel of Fig. 2 also shows that the rate of energy release, reflected by the slopes of the curves, decreases as M_{DM} increases, which implies that the time needed for a WD to reach the same amount of burnt matter increases. We list the mass fractions of major elements at the end of the simulations in Table 2. In general, the amounts of unburnt fuel and IME increase with M_{DM} , while those of iron-peaked elements drop. For example, the unburnt ^{12}C are about 34% and 46% of the total mass for models 2D-PTD-3-0-c3 ($M_{\text{DM}} = 0$) and 2D-PTD-3-3-c3 ($M_{\text{DM}} = 0.03M_\odot$), respectively. On the other hand, the mass fraction of ^{56}Ni decreases significantly from about 24% to 2.8% as M_{DM} increases from 0 to $0.03M_\odot$. This is related to the different initial density distributions in the models. For a larger M_{DM} , the amount of matter that can reach sufficiently high density for complete combustion decreases.

Next we consider the effects of DM on the flame surface. We plot in Figs. 3-6 the flame surfaces (represented by the temperature) at $t = 1 \text{ s}$ for the models listed in Table 1. In Model 2D-PTD-3-0-c3, which is the standard PTD model without DM considered in the literature (see for example Niemeyer & Woosley (1997), Reinecke et al. (1999a) and Reinecke et al. (2002a)), the flame shows a convoluted structure, with clear instabilities of flame-fluid interaction including the Rayleigh-Taylor instabilities and Kelvin-Helmholtz instabilities. The injection of fuel into the flame can be seen as well. When M_{DM} increases, the injection of fuel can still be found. But the

Table 1

Simulation setup for four PTD models: central densities of NM $\rho_{c(\text{NM})}$ and DM $\rho_{c(\text{DM})}$ are in units of 10^9 g cm^{-3} . Masses of the baryonic matter M_{NM} , dark matter M_{DM} , and the final nickel-56 mass M_{Ni} are in units of solar mass. R is the initial stellar radius. E_{nuc} and E_{tot} are the energy released by nuclear reactions and final total energy, respectively, both in units of 10^{50} erg . We assume $m_{\text{DM}} = 1 \text{ GeV}$.

Model	$\rho_{c(\text{NM})}$	$\rho_{c(\text{DM})}$	M_{NM}	M_{DM}	R (km)	M_{Ni}	E_{nuc}	E_{tot}
2D-PTD-3-0-c3	3.0	0.0	1.377	0.00	1.92×10^3	0.33	7.2	2.1
2D-PTD-3-1-c3	3.0	150	1.313	0.01	2.22×10^3	0.25	5.8	1.5
2D-PTD-3-2-c3	3.0	530	1.223	0.02	2.79×10^3	0.14	3.9	0.46
2D-PTD-3-3-c3	3.0	1050	1.015	0.03	4.25×10^3	2.9×10^{-2}	1.1	-0.85

Table 2

Mass fractions (normalized by the stellar mass) of all isotopes at the end of the simulations for the models listed in Table 1.

Isotope	2D-PTD-3-0-c3	2D-PTD-3-1-c3	2D-PTD-3-2-c3	2D-PTD-3-3-c3
^{12}C	0.30	0.32	0.36	0.43
^{16}O	0.33	0.35	0.39	0.46
^{24}Mg	1.4×10^{-2}	1.4×10^{-2}	1.4×10^{-2}	1.0×10^{-3}
^{28}Si	5.2×10^{-2}	5.9×10^{-2}	4.9×10^{-3}	3.9×10^{-2}
^{32}S	1.8×10^{-2}	1.9×10^{-2}	1.6×10^{-2}	1.1×10^{-2}
^{36}Ar	3.2×10^{-3}	3.1×10^{-3}	2.5×10^{-3}	1.7×10^{-3}
^{40}Ca	3.1×10^{-3}	2.9×10^{-3}	2.3×10^{-3}	1.3×10^{-3}
^{44}Ti	6.5×10^{-6}	9.6×10^{-6}	7.3×10^{-6}	2.4×10^{-6}
^{48}Cr	1.5×10^{-4}	1.4×10^{-4}	8.8×10^{-4}	2.3×10^{-5}
^{52}Fe	4.8×10^{-3}	3.8×10^{-3}	2.3×10^{-3}	5.1×10^{-4}
^{54}Fe	5.1×10^{-2}	4.5×10^{-2}	3.3×10^{-2}	1.7×10^{-2}
^{56}Ni	0.22	0.18	0.11	2.8×10^{-2}

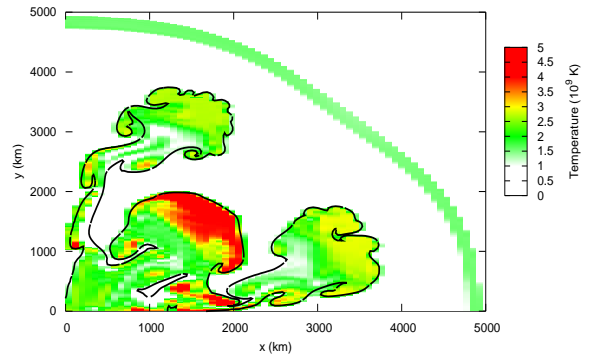
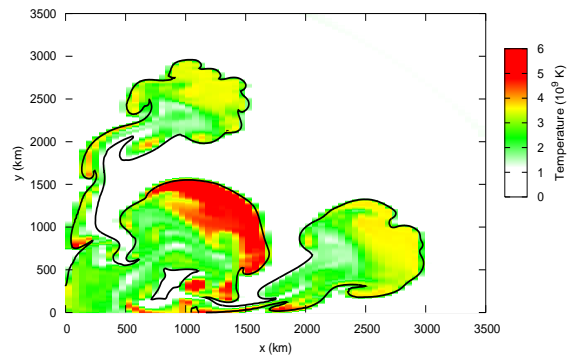
Kelvin-Helmholtz instabilities are suppressed. The flame surface also becomes smoother and less turbulent.

3.2. Connection with Sub-luminous Supernovae

The light curve of a sub-luminous SNIa has a low peak luminosity, suggesting that the ^{56}Ni content is lower than ordinary SNIa. The explosion is very weak and only partial ejecta are dispelled instead of a disruption of the whole star. Notice that, how much and how the mass is ejected in the explosion are not clear unless the simulation continues until the homologous expansion phase is reached, which takes place about ten seconds after the deflagration/detonation stage has ended (Roepke & Hillebrandt 2005; Roepke 2005). However, this involves using either a sufficiently large simulation box which can accommodate the rapidly expanding ejecta or expanding meshes to prevent the ejecta from leaving the box (Roepke 2005).

Since the amount of ejecta mass is an important parameter in constructing the resultant light curves from the simulations, we constrain it in the following ways. First the minimum ejecta mass is estimated by counting all the fluid elements with positive energy at the end of the simulation. Second we assume that the maximum ejecta mass is equal to the total mass of the star.

In Fig. 7 we show the bolometric light curves for the four simulation models listed in Table 1 (from the top solid line to the next-to-bottom solid line) and also one additional model (the bottom line) not listed in the table. The extra model has a DM core mass $M_{\text{DM}} = 0.032 M_{\odot}$. For the first three models (2D-PTD-3-0-c3, 2D-PTD-3-1-c3, 2D-PTD-3-2-c3), the total final energies are positive and hence we use the maximum ejecta mass for each model to construct the light curves. On the other hand, we use the minimum ejecta mass to construct the light curves for the remaining two models because their total

**Figure 3.** The flame surface of Model 2D-PTD-3-0-c3 at $t = 1 \text{ s}$.**Figure 4.** Same as Fig. 3, but for Model 2D-PTD-3-1-c3.

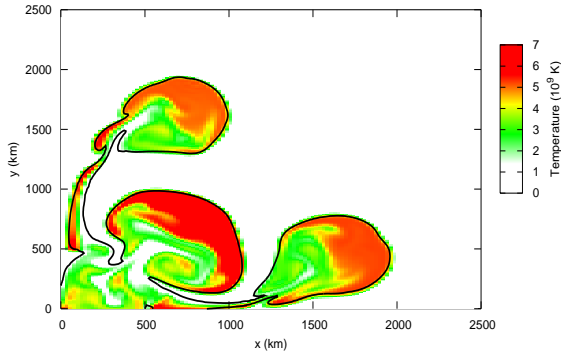


Figure 5. Same as Fig. 3, but for Model 2D-PTD-3-2-c3.

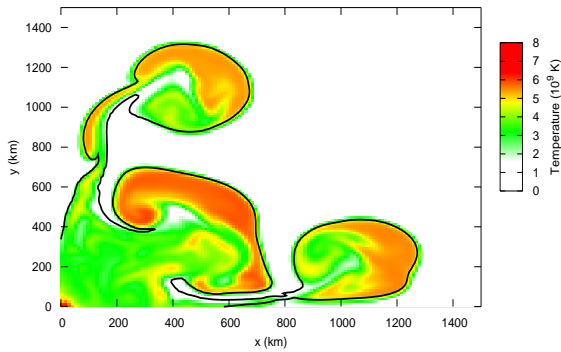


Figure 6. Same as Fig. 3, but for Model 2D-PTD-3-3-c3.

final energies are negative. Fig. 7 shows that the peak luminosity depends sensitively on M_{DM} . In particular, it can decrease by almost two orders of magnitude as M_{DM} increases from 0 to $0.032M_{\odot}$. In the figure, we also plot the data from the constructed bolometric light curves for some examples of sub-luminous SNIa for comparison. It can be seen that our SNIa simulations with admixed DM give a range of peak luminosities that covers the observed sub-luminous SNIa including the exceptionally dim SN2008ha.

Our results suggest that the variations of the observed light curves of different sub-luminous SNIa may be due to the fact that the underlying WDs of the systems contain different amounts of DM. For a given observed SNIa light curve, we can use M_{DM} as a parameter for performing hydrodynamical simulations to fit the observed data. In principle, for a given M_{DM} , a unique light curve can be determined by the resulting velocity profile and total mass of ejecta obtained from the simulation. However, as we discussed above, the total mass of ejecta cannot be determined accurately from the simulations due to computational limitations. We thus calculate two different light curves corresponding to the minimum and maximum ejecta masses for a chosen M_{DM} .

In Fig. 8 we plot the bolometric light curves by using the results from a simulation model with $M_{\text{DM}} = 0.02M_{\odot}$. The solid and dashed lines in the figure are

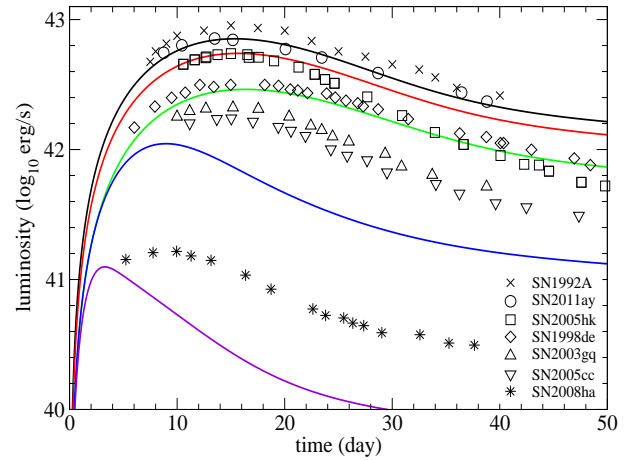


Figure 7. From the top solid line to the next-to-bottom solid line: bolometric light curves of Models 2D-PTD-3-0-c3, 2D-PTD-3-1-c3, 2D-PTD-3-2-c3 and 2D-PTD-3-3-c3. The lowest light curve corresponds to an extra model, with similar configurations as the above four models but with $M_{\text{DM}} = 0.032M_{\odot}$. Observational data of SN2011ay, SN2005hk, SN1999by, SN2003gq, SN2005cc and SN2008ha are included.

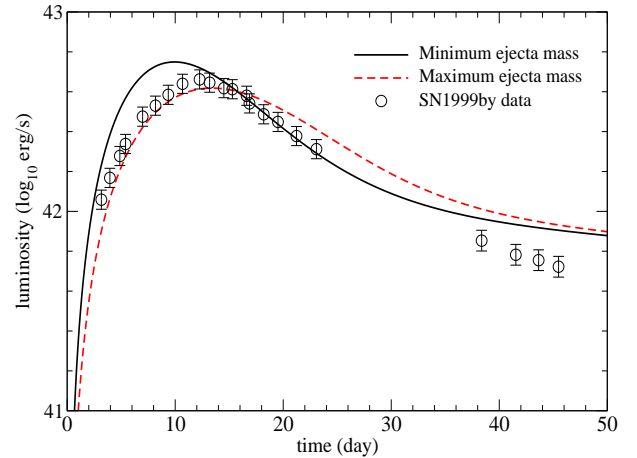


Figure 8. Bolometric light curves of a simulation model with $M_{\text{DM}} = 0.02M_{\odot}$. The solid (dashed) line is constructed by assuming that the ejecta mass takes the minimum (maximum) value estimated from the simulation as discussed in the text. Observational data of SN1999by is also included. The error bars correspond to the uncertainties in the distance modulus and the measurements.

obtained by using the minimum and maximum ejecta masses, respectively. This simulation model has a positive total final energy. As a result, the minimum and maximum ejecta masses estimated from the simulation are comparable, and hence the two constructed light curves are also quite close to each other. We expect that the light curve corresponding to the actual ejecta mass should lie between the two limits. In the figure, the observational data of a sub-luminous supernova SN1999by (with error bars) are also presented for comparison. The error bars correspond to the uncertainties in the distance modulus and measurements. It is seen that the data around the peak luminosity lie very close to the region between the two constructed theoretical light curves, which represents effectively our uncertainty in the calculation. At later time, the observational data decays faster than the theoretical light curves. One possible reason may be that our assumption of the opacity law and gamma-ray deposition function are no longer valid at later time.

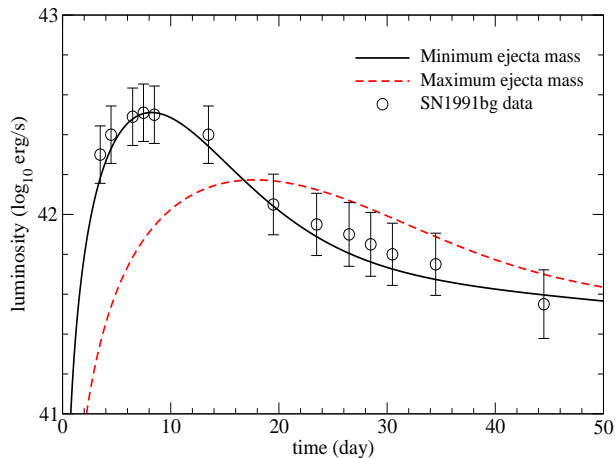


Figure 9. Same as Fig. 8 but for a simulation model with $M_{\text{DM}} = 0.026M_{\odot}$. Observational data of SN1991bg is included for comparison. The error bars correspond to the uncertainties in the distance modulus and the measurements.

As a different example, we plot in Fig. 9 the bolometric light curves of a simulation model with $M_{\text{DM}} = 0.026M_{\odot}$. Contrary to the simulation model with $M_{\text{DM}} = 0.02M_{\odot}$ discussed above, this model has a negative total final energy and hence the estimated minimum ejecta mass differs from the maximum ejecta mass quite significantly. As a result, the two corresponding light curves (solid and dashed lines) are not close to each other. In the figure, the observational data of another sub-luminous supernova SN1991bg is also plotted, which agrees quite well with the theoretical light curve constructed with the minimum ejecta mass.

The above examples show that the admixture of dark matter can produce SNIa light curves with large variations in peak luminosities comparable with those of sub-luminous SNIa. M_{ej} also affects the peak luminosity, but its influence is much less pronounced than M_{DM} . On the other hand, M_{ej} dominates the width of a light curve. This suggests that the observational data of an SNIa can provide hint on the ejecta mass and its admixed DM mass, with M_{DM} determining the peak luminosity while M_{ej} the light curve width. Given the light curve data of an SNIa, we search for the best-fitted pair of M_{DM} and M_{ej} , where the values of M_{Ni} and v_{ej} are derived from simulations as functions of M_{DM} . Models with the minimum chi-squared values are chosen to be the representing models of that SNIa. In Table 3 we list the models with minimum chi-squared values of several well observed sub-luminous SNIa. The table lists the agreeing M_{ej} , M_{DM} with their implied M_{Ni} , ejecta velocity v_{ej} and the two ejecta mass limits $M_{\text{ej}}(\text{max})$ and $M_{\text{ej}}(\text{min})$, which are derived from simulations. We regard that the DM admixture of this model can be a possible explanation of an observed sub-luminous SNIa if its fitted M_{ej} lies within the two limits of M_{ej} . All sub-luminous SNIa in the list except SN1991bg and SN1993H give an M_{ej} inside the two limits, showing that these SNIa could possibly have admixed DM cores in the WD progenitors. The SN1993H (SN1991bg) has an ejecta mass just above (below) the upper (lower) M_{ej} limit, showing that the observational data is declining slower (faster) than what the current configuration can provide.

In Fig. 10 we plot the peak-luminosity against the fitted M_{DM} of the mentioned SNIa. The peak luminosities

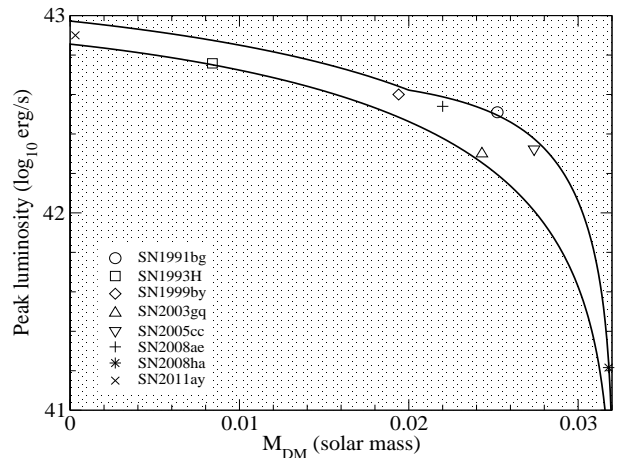


Figure 10. The SNIa peak-luminosity against M_{DM} . Peak luminosities of some observed SNIa are also plotted. The shaded regions are excluded by the mass bounds of the progenitor mass and minimum ejecta mass derived from simulations.

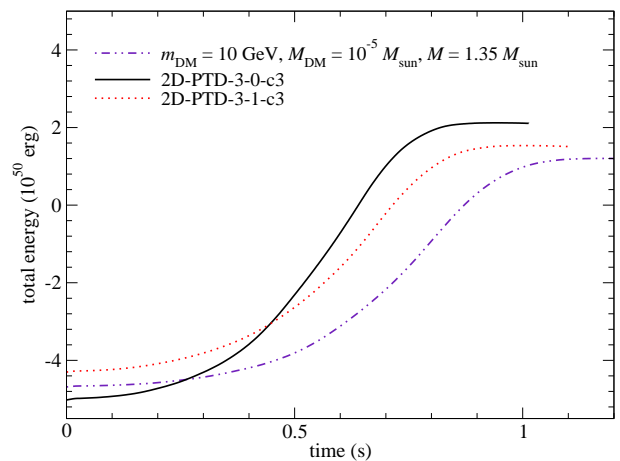


Figure 11. Total energy against time for Models 2D-PTD-3-0-c3, 2D-PTD-3-1-c3 and an extra model similar to Model 2D-PTD-3-1-c3 but with $M_{\text{DM}} = 10^{-5}M_{\odot}$ and $m_{\text{DM}} = 10 \text{ GeV}$.

of some observed SNIa are included as data points. The shaded regions of the plot are excluded by this model because these regions correspond to models with an ejecta mass out of the bounds. Given an M_{DM} the range of peak luminosities is very small compared to the observed range of SNIa peak luminosities. This implies that the admixed DM mass can be well constrained by the peak luminosity.

In summary, our work shows that the admixture of DM can explain the observation data of sub-luminous SNIa. However, as discussed in Sec. 1, it should be noted that matching of the bolometric light curves of sub-luminous SNIa can also be achieved in other models (Pakmor et al. 2010; Kromer et al. 2013a,b; Fink et al. 2014; Kromer et al. 2015).

4. CONCLUSION

In this paper, we have performed two-dimensional Newtonian hydrodynamic simulations to study the effects of DM on the thermonuclear explosion of WDs near the Chandrasekhar mass limit. Our initial models are constructed by solving the two-fluid hydrostatic equilibrium equations for NM and DM with a fixed central NM density of $3 \times 10^9 \text{ g cm}^{-3}$, which is expected to be near

Table 3

Fitting results of observed sub-luminous SNIa. Masses are in units of solar mass and the ejecta velocity v_{ej} are in units of 10^9 cm s $^{-1}$. $M_{ej (max)}$ and $M_{ej (min)}$ are the maximum and minimum ejecta masses derived from simulations. The last column marks the possibility of using admixed DM to explain the observed SNIa. $m_{DM} = 1$ GeV is assumed.

Supernova	M_{DM}	M_{ej}	M_{Ni}	v_{ej}	$M_{ej (max)}$	$M_{ej (min)}$	DM origin
SN1991bg	0.025	0.20	0.084	0.44	1.14	0.21	No
SN1993H	0.008	1.37	0.216	0.74	1.35	0.69	No
SN1999by	0.019	0.61	0.148	0.58	1.24	0.54	Yes
SN2003gq	0.024	0.82	0.094	4.61	1.16	0.25	Yes
SN2005cc	0.027	0.33	0.058	3.70	1.01	0.14	Yes
SN2008ae	0.022	0.67	0.120	5.22	1.20	0.38	Yes
SN2008ha	0.032	0.12	0.004	2.19	1.00	0.09	Yes
SN2011ay	0.000	1.35	0.320	7.63	1.38	0.73	Yes

the minimum density for triggering the explosion. The typical models studied by us are solar-mass WDs with small DM cores ($\sim 0.01M_{\odot}$) formed by DM with a particle mass of 1 GeV. As a first step towards understanding the effects of DM on SNIa, we assume that the DM core is stationary during the evolution, and we only model the dynamics of the NM fluid. This should be a good approximation as the DM core should be affected mainly by its self-gravity due to its high compactness. We employ the PTD model as the explosion mechanism and use the standard level-set method to model the flame surface during the dynamical evolution.

We have only considered the PTD model as the explosion mechanism in this work. It would be interesting to extend our work by using other possible explosion mechanisms such as the DDT and GCD models as discussed in Sec. 1. Finally, we have also assumed that the DM core is formed by non-self-annihilating fermionic DM with particle mass 1 GeV. How would our results be changed if one considers much more massive DM particle candidates? We plot in Fig. 11 the total energy against time for Models 2D-PTD-3-0-c3, 2D-PTD-3-1-c3 and an extra model similar to Model 2D-PTD-3-1-c3 but with $M_{DM} = 10^{-5}M_{\odot}$ and $m_{DM} = 10$ GeV. The initial mass of the extra model is $1.35 M_{\odot}$. Despite the small M_{DM} in the new case, the effects of DM on the energy release during explosion is comparable with Model 2D-PTD-3-1-c3, which has $M_{DM} = 0.01M_{\odot}$. As found in our previous work Leung et al. (2013), for the same M_{DM} or central density, a higher m_{DM} has a stronger effect on the density profile comparing to the case of $m_{DM} = 1$ GeV. It is because the DM core is more compact and creates a stronger gravitational attraction field, which changes the initial density profile more significantly. These changes in the density profiles are also reflected by the drop of energy release in SNIa explosions. Our results show that SNIa explosions are sensitive to both the drop of Chandrasekhar mass, as shown in the 1 GeV case, and to the particle mass. However, modeling more massive DM core with $m_{DM} = 10$ GeV is difficult because the region expected to be admixed with DM will be even smaller, implying that a much higher resolution is needed in order to model both DM and NM consistently.

Our numerical results show that an increase in M_{DM} or m_{DM} leads to a change in the SNIa explosion by either decreasing the Chandrasekhar limit for low m_{DM} or altering the density profile for high m_{DM} . First, the explosion becomes weaker and the total energy release is reduced. The total turbulence energy, which is an important in-

dicator for the PTD model, also decreases. Second, the amounts of unburnt fuel and IME increase, while those of iron-peaked elements decrease. In particular, the total mass of ^{56}Ni depends quite sensitively on M_{DM} and decreases from about 0.3 to $0.03M_{\odot}$ as M_{DM} increases from 0.01 to $0.03M_{\odot}$ for the $m_{DM} = 1$ GeV case. Finally, the Kelvin-Helmholtz instabilities are suppressed and the flame surface also becomes smoother and less turbulent as M_{DM} increases. We have also constructed the bolometric light curves from our simulations and compared them with the observational data of sub-luminous SNIa. Our results shows that varying the DM core mass from about 0.01 to $0.03M_{\odot}$ yields a range of peak luminosities that covers the observational data very well. The variations of the observed light curves of different sub-luminous SNIa may be due to the fact that the precursor WDs contain different amounts of DM.

5. ACKNOWLEDGMENT

We thank F. X. Timmes for his open-source subroutines for the Helmholtz equation of state, nuclear reaction network and the neutrino emission luminosity. This work is partially supported by a grant from the Research Grant Council of the Hong Kong Special Administrative Region, China (Project No. 400910) and a CUHK Direct Grant 4053069. SCL is supported by the Research Grant Council of the Hong Kong Government through the Hong Kong PhD Fellowship Scheme.

REFERENCES

- Aalseth, C. E., et al. 2011, Phys. Rev. Lett., 106, 131301
 Arnett, W. D. 1969, Ap & SS, 5, 180
 —. 1982, Astrophys. J., 253, 785
 Barth, T. J., & Deconinck, H. 1999, Lecture Notes in Computational Science and Engineering 9: High-Order Methods for Computational Physics (Springer)
 Benetti, S., et al. 2005, Astrophys. J., 623, 1011
 Bernabei, R., et al. 2013, Int. J. Mod. Phys. A, 28, 1330022
 Bertone, G., & Fairbairn, M. 2008, Phys. Rev. D, 77, 043515
 Bramante, J., Fukushima, K., & Kumar, J. 2013, Phys. Rev. D, 87, 055012
 Branch, D., & Tammann, T. A. 1992, Ann. Rev. Astron. Astrophys., 30, 359
 de Lavallaz, A., & Fairbairn, M. 2010, Phys. Rev. D, 81, 123521
 Doull, B. A., & Baron, E. 2011, Publ. Astron. Soc. Pac., 123, 765
 Fairbairn, M., Scott, P., & Edsjo, J. 2008, Phys. Rev. D, 77, 047301
 Fan, Y.-Z., Yang, R.-Z., & Chang, J. 2011, Phys. Rev. D, 84, 103510
 Filippenko, A. V., et al. 1992, Astron. J., 104, 1543
 Fink, M., et al. 2009, Astron. Astrophys., 514, A53
 —. 2014, Mon. Not. R. astr. Soc., 438, 438

- Foley, R. J., et al. 2009, *Astron. J.*, 138, 376
— 2014, *Astrophys. J.*, 792, 29
Freese, K., Spolyar, D., Bodenheimer, P., & Gondolo, P. 2009, arXiv:0903.0101v1
Gamezo, V. N., Khokhlov, A. M., & Oran, E. S. 2004, *Phys. Rev. Lett.*, 92, 211102
— 2005, *Astrophys. J.*, 623, 337
Goldman, I., & Nussinov, S. 1989, *Phys. Rev. D*, 40, 3221
Gonzalez, D., & Reisenegger, A. 2010, *Astron. Astrophys.*, 522, A16
Gould, A. 1987a, *Astrophys. J.*, 321, 571
— 1987b, *Astrophys. J.*, 321, 560
— 1988, *Astrophys. J.*, 328, 919
Hirano, S., Umeda, H., & Yoshida, N. 2011, *Astrophys. J.*, 736, 58
Hoeflich, E., & Khokhlov, A. M. 1996, *Astrophys. J.*, 457, 500
Hoeflich, P., et al. 1996, *Astrophys. J.*, 472, L81
Hooper, D., Spolyar, D., Vallionotto, A., & Gnedin, N. Y. 2012, *Phys. Rev. D*, 81, 103531
Iwamoto, K., et al. 1999, *Astrophys. J. Suppl.*, 125, 439
Jordan, G. C. I., et al. 2008, *Astrophys. J.*, 681, 1448
— 2012, *Astrophys. J.*, 759, 53
Kasen, D., & Plewa, T. 2007, *Astrophys. J.*, 662, 459
Khokolov, A. M. 1989, *Mon. Not. R. astr. Soc.*, 239, 785
Khokhlov, A. M. 1991a, *Astron. Astrophys.*, 245, 114
— 1991b, *Astron. Astrophys.*, 245, L25
— 1991c, *Astrophys. J.*, 246, 383
Khokhlov, A. M., Oran, E. S., & Wheeler, J. C. 1997, *Astrophys. J.*, 478, 678
Kouvaris, C. 2008, *Phys. Rev. D*, 77, 023006
— 2012, *Phys. Rev. Lett.*, 108, 191301
Kouvaris, C., & Tinyakov, P. 2010, *Phys. Rev. D*, 82, 063521
— 2011, *Phys. Rev. D*, 83, 083512
Kromer, M., et al. 2010, *Astrophys. J.*, 719, 1067
— 2013a, *Mon. Not. R. astr. Soc.*, 429, 2287
— 2013b, *Astrophys. J.*, 778, L18
— 2015, *Mon. Not. R. astr. Soc.*, 450, 3045
Leibundgut, B., & Pinto, P. A. 1992, *Astrophys. J.*, 401, 49
LeSaffre, P., Han, Z., Tout, C. A., Podsiadlowski, P., & Martin, R. G. 2006, *MNRAS*, 368, 187
Leung, S.-C., Chu, M.-C., & Lin, L.-M. 2011, *Phys. Rev. D*, 84, 107301
— 2012, *Phys. Rev. D*, 85, 103528
— 2015, arXiv:1507.08549
Leung, S.-C., Chu, M.-C., Lin, L.-M., & Wong, K.-W. 2013, *Phys. Rev. D*, 87, 123506
Li, W., et al. 2001, *Astrophys. J.*, 546, 734
Lisewski, A. M., Hillebrandt, W., & Woosley, S. E. 2000, *Astrophys. J.*, 538, 831
Livne, E., & Glasner, A. S. 1990, *Astrophys. J.*, 361, 244
Long, M., et al. 2014, *Astrophys. J.*, 789, 103
McDermott, S. D., Yu, H.-B., & Zurek, K. M. 2012, *Phys. Rev. D*, 85, 023519
- Meakin, C. A., et al. 2009, *Astrophys. J.*, 693, 1188
Moll, R., & Woosley, S. E. 2013, *Astrophys. J.*, 774, 137
Moskalenko, I. V., & Wai, L. L. 2007, *Astrophys. J.*, 659, L29
Niemeyer, J. C., & Hillebrandt, W. 1995, *Astrophys. J.*, 452, 769
Niemeyer, J. C., & Woosley, S. E. 1997, *Astrophys. J.*, 475, 740
Nomoto, K. 1982a, *Astrophys. J.*, 253, 798
— 1982b, *Astrophys. J.*, 257, 780
Nomoto, K., Sugimoto, D., & Neo, S. 1976, *Ap & SS*, 39, 37
Nomoto, K., Thielemann, F.-K., & Yokoi, K. 1984, *Astrophys. J.*, 286, 644
Pakmor, R., Kromer, M., Taubenberger, S., & Spiegel, V. 2013, *Astrophys. J.*, 770, L8
Pakmor, R., et al. 2010, *Nature*, 463, 61
Paxton, B., et al. 2011, *Astrophys. J. Suppl.*, 192, 3
— 2013, *Astrophys. J. Suppl.*, 208, 4
— 2015, arXiv:1506.03146
Perez-Garcia, M. A., & Silk, J. 2014, arXiv:1403.6111
Perlmutter, S., et al. 1999, *Astrophys. J.*, 517, 565
Plewa, T. 2007, *Astrophys. J.*, 657, 942
Reinecke, M., Hillebrandt, W., & Niemeyer, J. C. 1999a, *Astron. Astrophys.*, 347, 739
— 2002a, *Astron. Astrophys.*, 386, 936
— 2002b, *Astron. Astrophys.*, 391, 1167
Reinecke, M., Hillebrandt, W., Niemeyer, J. C., Klein, R., & Gloebl, A. 1999b, *Astron. Astrophys.*, 347, 724
Riess, A. G., et al. 1998, *Astron. J.*, 116, 1009
Ripamonti, E., et al. 2010, *Mon. Not. Roy. Astron. Soc.*, 406, 2605
Roepke, F. K. 2005, *Astron. Astrophys.*, 432, 969
Roepke, F. K., Gieseler, M., Reinecke, M., Travaglio, C., & Hillebrandt, W. 2006, *Astron. Astrophys.*, 453, 203
Roepke, F. K., & Hillebrandt, W. 2005, *Astron. Astrophys.*, 431, 635
Roepke, F. K., Hillebrandt, W., & Woosley, S. E. 2007, *Astrophys. J.*, 660, 1344
Ruiter, A. J., et al. 2011, *Mon. Not. R. astr. Soc.*, 417, 408
— 2014, *Mon. Not. R. astr. Soc.*, 440, L101
Ruiz-Lapuente, P., et al. 1993, *Nature*, 365, 728
Scalzo, R. A., Ruiter, A. J., & Sim, S. A. 2014, *Mon. Not. R. astr. Soc.*, 445, 2535
Seitenzahl, I. R., Ciaraldi-Schoolmann, F., & Roepke, F. K. 2011, *MNRAS*, 414, 2709
Seitenzahl, I. R., et al. 2013, *Mon. Not. R. astr. Soc.*, 429, 1156
Sim, S. A. 2010, *Astrophys. J.*, 714, L52
Sim, S. A., et al. 2012, *Mon. Not. R. astr. Soc.*, 420, 3003
Spolyar, D., et al. 2008, *Phys. Rev. Lett.*, 100, 051101
— 2009, *Astrophys. J.*, 705, 1031
Timmes, F. X. 1999, *Astrophys. J.*, 124, 241
Timmes, F. X., & Arnett, D. 1999, *Astrophys. J.*, 125, 277
Timmes, F. X., & Swesty, F. D. 1999, *Astrophys. J. Suppl.*, 126, 501
Woosley, S. E. 1997, *Astrophys. J.*, 476, 801
Woosley, S. E., & Weaver, T. A. 1994, *Astrophys. J.*, 423, 371

6. APPENDIX: EFFECTS OF DM ADMIXTURE ON SNIA PROGENITORS

In this article we have studied how the gravity of DM affects the explosion energetics of SNIa. We have shown that with an admixed DM core with a total mass in the order of $\sim 10^{-2}M_{\odot}$, the ^{56}Ni production can be significantly suppressed and the corresponding light curves are comparable with those of sub-luminous SNIa. However, it remains unclear whether such a DM admixture can leave observable consequences already during the main-sequence phase, which is well constrained by observational data. Therefore, it is necessary to check if stars with DM admixture have unusual evolution paths that are inconsistent with observational data, and if the chemical compositions of the resultant white dwarfs are different from those of conventional cases.

A star acquires DM mainly by accretion through DM-NM scattering or by its inherent admixture that exists already during its formation stage, where DM acts as a

stellar seed. However, following (Kouvaris 2008) to estimate the DM accretion rate, using conventional DM parameters, the typical DM accretion rate is insignificant compared with the original mass of the star, even when we consider a duration of cosmological timescale. Therefore, it is unlikely that a star can acquire DM with a mass comparable with the host simply by accretion. We thus focus on DM which acts as a stellar seed. In that case, the gravity of DM is important even in the protostellar phase.

We performed main-sequence star simulations by using an open-source stellar evolution code MESA (Modules for Experiments in Stellar Astrophysics) (Paxton et al. 2011, 2013, 2015), which can follow the evolution of a star from the protostellar phase up to the white dwarf stage. We used the MESA code version 3372, which solves the fully coupled one-dimensional structure and composition equations simultaneously, using the Helmholtz EOS to describe the thermodynamics properties of NM. The DM

Table 4

Stellar properties at the end of simulations and main-sequence lifetime for models with $M_{\text{NM}} = 4$ or $7M_{\odot}$. M_{He} and M_{CO} are the masses of ${}^4\text{He}$, ${}^{12}\text{C}$ and ${}^{16}\text{O}$ in units of solar mass. X_{C} and X_{O} are the mass fractions of ${}^{12}\text{C}$ and ${}^{16}\text{O}$ of the innermost mass shell. $T_{\text{H start}}$ ($T_{\text{H end}}$) and $T_{\text{He start}}$ ($T_{\text{He end}}$) are the beginning (ending) time for hydrogen and helium burning in units of years.

M_{NM}	M_{DM}	M_{He}	M_{CO}	X_{C}	X_{O}	$T_{\text{H start}}$	$T_{\text{H end}}$	$T_{\text{He start}}$	$T_{\text{He end}}$
4	0	0.24	0.18	0.40	0.58	1.12×10^6	1.49×10^8	1.55×10^8	1.89×10^8
4	0.01	0.24	0.19	0.47	0.50	1.08×10^6	1.46×10^8	1.50×10^8	1.82×10^8
4	0.02	0.18	0.37	0.56	0.42	1.05×10^6	1.44×10^8	1.47×10^8	1.82×10^8
4	0.03	N/A	N/A	N/A	N/A	1.01×10^6	1.44×10^8	1.47×10^8	N/A
7	0	0.32	0.13	0.44	0.54	2.30×10^5	3.98×10^7	4.05×10^7	4.70×10^7
7	0.01	0.31	0.13	0.44	0.54	2.30×10^5	3.98×10^7	4.05×10^7	4.70×10^7
7	0.02	0.31	0.13	0.47	0.50	2.20×10^5	3.92×10^7	3.96×10^7	4.57×10^7
7	0.03	N/A	N/A	N/A	N/A	2.19×10^5	3.94×10^7	N/A	N/A

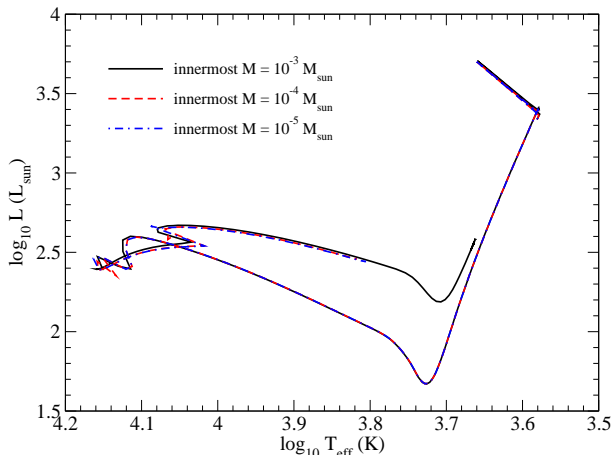


Figure 12. The H-R diagrams of stars with $4 M_{\odot}$ NM and $0.03 M_{\odot}$ DM but with different innermost mass shell. The simulation is done until the time-step becomes smaller than 10^1 years.

is assumed to be in hydrostatic equilibrium, and to a good approximation, the DM profile remains static during the simulation. We observed that due to the compactness of the DM core, in most of the stellar lifetime, the DM core has a size smaller than the outer radius of the innermost fluid elements. Effectively, we modified the hydrostatic equation in the MESA code by including the DM core which behaves like a point-mass as

$$\frac{dP_{\text{NM}}}{dm} = -\frac{G(m_{\text{NM}}(r) + M_{\text{DM}})}{4\pi r^4}. \quad (10)$$

All notations have the same meaning as those in the main text. Due to the singular behavior of the DM potential near the core, there are numerical difficulties that the results are resolution dependent. Also, the typical time-step becomes prohibitively small, due to the large potential gradient, which leads to a large density gradient and hence a large chemical composition gradient near the core. Also, the $1/r$ potential from the DM leads to divergence in constructing the initial model. To ameliorate these problems, we smear out the effect of DM by increasing the innermost fluid elements from 10^{-8} to $10^{-4}M_{\odot}$. This allows us to capture the effects of DM's gravity within a reasonable simulation time.

We use the star evolution model `1M_pre_ms_wd` in the *test suite* package to follow the stellar evolution from the protostellar phase. We considered star models with a mass from 4 to $7 M_{\odot}$, which are believed to be the progenitors of carbon-oxygen white dwarfs.

To show that the rise of innermost fluid element mass

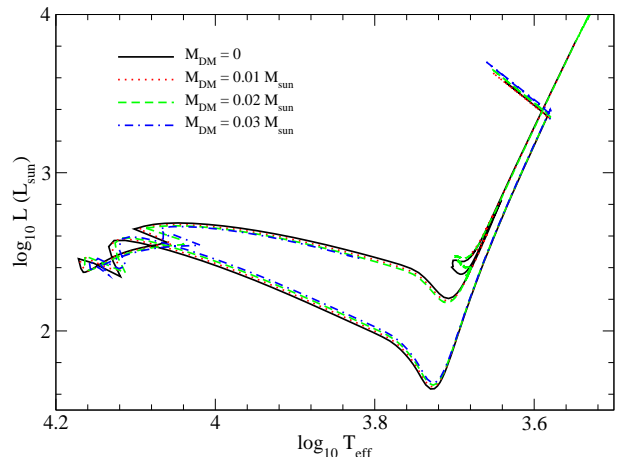


Figure 13. The H-R diagrams of stars with $4 M_{\odot}$ NM. M_{DM} ranges from 0 to $0.03 M_{\odot}$. All simulations have the innermost mass shell fixed at $10^{-4}M_{\odot}$, and they are stopped when the time-step becomes smaller than 10^1 years.

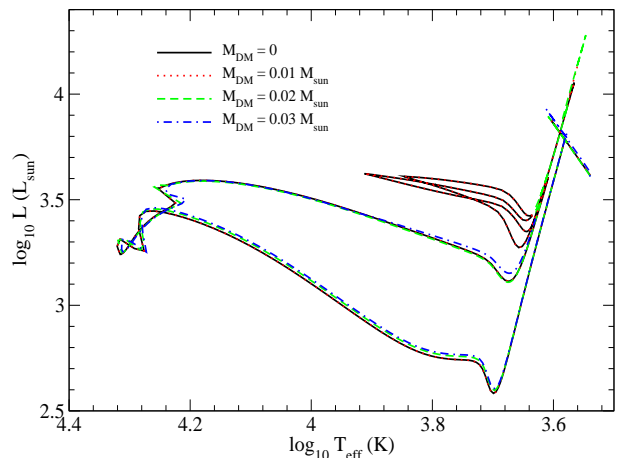


Figure 14. Same as Fig. 13, but for $M_{\text{NM}} = 7M_{\odot}$.

does not introduce spurious results, we plot in Fig. 12 the HR diagram of a star with $4 M_{\odot}$ NM and $0.03 M_{\odot}$ DM, but with different innermost fluid element masses. We do not follow the whole evolution till the formation of the white dwarf because the timestep has already become prohibitively small when it enters the helium burning phase. We stopped the simulation when the average time step drops below 10^1 years. In the mass range considered, the qualitative behavior of the stellar evolution remains unchanged. This shows that in this resolution

the basic properties of the main-sequence phase are captured. The model with a higher innermost mass shell can run longer due to the stronger smearing of the DM point-mass gravity.

We plot in Figs. 13 and 14 the HR diagrams for star models with a normal matter mass of 4 and 7 solar masses, but for different M_{DM} . In both figures, the evolution paths of the hydrogen burning phase and the helium burning phase are insensitive to M_{DM} . We terminated the simulations for $M_{\text{DM}} = 0.03M$ before the exhaustion of core helium because of the small time-steps. One qualitative difference that can be observed is the disappearance of the horizontal branch during helium burning for the model with $M_{\text{NM}} = 7M_{\odot}$ and $M_{\text{DM}} = 0.02M_{\odot}$.

In Table 4 we tabulate the stellar properties extracted from profiles at the end of simulations, and also the age of the star when hydrogen or helium burning starts or ends. No results are listed for models with $M_{\text{DM}} = 0.03M_{\odot}$ because the simulations are terminated before the helium burning phase commences. For models with $M_{\text{NM}} = 4M_{\odot}$, when M_{DM} increases, the helium mass decreases

while the carbon-oxygen mass increases. Also, hydrogen burning begins and ends sooner, with the whole hydrogen burning lifetime shortened. Similar features are observed for the helium burning. The ^{12}C mass fraction increases while that of ^{16}O decreases. The effects of DM in models with $M_{\text{NM}} = 7M_{\odot}$ become smaller so that there is almost no change when $M_{\text{DM}} = 0.01M_{\odot}$. But as M_{DM} further increases, similar effects can still be observed, including a lower helium mass, earlier hydrogen and helium burning and a shorter main-sequence lifetime. Also, an increase (a decrease) in ^{12}C (^{16}O) mass fraction is observed.

From the above comparison, we have shown that in the mass range of M_{DM} considered in the main text, the DM core which is assumed to exist as early as the star forms, does not alter the stellar evolution significantly. Specifically, all models predict a path during the main-sequence phase in the HR diagram comparable with the cases without DM. Moreover, the final chemical composition of the carbon-oxygen white dwarf does not deviate significantly from what we have assumed, a 50 % carbon and 50 % oxygen by mass.